



Crashworthiness optimization of cylindrical negative Poisson's ratio structures with inner liner tubes

Qiang Gao¹ · Wei-Hsin Liao¹ · Liangmo Wang² · Chen Huang¹

Received: 30 September 2020 / Revised: 23 August 2021 / Accepted: 25 August 2021 / Published online: 7 September 2021
© The Author(s), under exclusive licence to Springer-Verlag GmbH Germany, part of Springer Nature 2021

Abstract

A novel structure with enhanced energy absorption is proposed by introducing thin-walled tube as the inner liner tube of the cylindrical structures with negative Poisson's ratio (C-NPR). The energy absorption performances of C-NPR structure with inner tube (C-NPR-IT) are compared to other configurations like the single NPR structure, single thin-walled tube, and C-NPR structure with outer tube (C-NPR-OT) to show its superiority. It is found that the interaction between the NPR structure and inner tube in C-NPR-IT can be enhanced. Then, the parametric analysis of the geometric parameters on the crashworthiness performance of C-NPR-IT structures are performed with finite element method. To achieve the best configuration, the surrogate modeling technique and the multi-objective particle swarm optimization (MOPSO) algorithm are employed to optimize the C-NPR-IT structures. The results show that the optimized structure improves the specific energy absorption (SEA) from 3.97 to 10.26 kJ/kg by almost 2.5× by controlling peak crushing force (PCF) less than 80 kN. Therefore, the C-NPR-IT structure has an application prospective in the energy absorber.

Keywords Auxetic structures · Crashworthiness · Thin-walled tube · Negative Poisson's ratio · Axial impact

1 Introduction

Auxetic structures with negative Poisson's ratio (NPR) and thin-walled structures are two kinds of structures applied in the energy absorption fields. NPR structures have attracted increasing attentions due to their unprecedented mechanical properties, such as indentation and impact resistance (Imbalzano et al. 2017; Jiang and Hu 2017), high shear modulus (Ren et al. 2018), and energy absorption capacity (Gao et al. 2019). They can contract when compressed to maximum material utilization and enhance the stiffness to absorb more energy. Thin-walled tubes are also applied because of its light weight and ease of design (Zhu et al. 2018a; b).

Various multi-cell configurations were introduced into the thin-walled tubes to improve the crashworthiness performance under axial and oblique impact loading (Murat Altin 2019; Murat Altin et al. 2019; Acar et al. 2019). Numerous optimization methods were employed to determine the geometric and material parameters of the energy absorbers (Mohammadiha and Ghariblu 2017; Xie et al. 2018; Xiong et al. 2018; Duan et al. 2019; Abdullahi and Gao 2020).

Auxetic behavior has been known since the beginning of the twentieth century. The Berlin researcher Karsten Pietsch invented the RFS structure (rhombic-fold structure) as the first artificially produced auxetic materials (Evans 1991). Lakes (Lakes 1987) manufactured the first foam structures with negative Poisson's ratio in 1987. Inspired by this, structures with various topological configurations have been proposed to achieve the unique properties. Mechanical properties and deformation mechanisms of the NPR structures have been studied comprehensively with analytical, numerical and experimental methods. Among various auxetic structures, the re-entrant hexagonal and double arrowed microstructures have been proven to possess higher Young's moduli (Elipse and Lantada 2012). Gibson and Ashby (Gibson and Ashby 1999) pioneered to develop the analytical model of the Young's modulus, shear modulus and yield

Responsible Editor: Erdem Acar

✉ Wei-Hsin Liao
whliao@cuhk.edu.hk

¹ Department of Mechanical and Automation Engineering, The Chinese University of Hong Kong, Shatin, Hong Kong, China

² Department of Automotive Engineering, School of Mechanical Engineering, Nanjing University of Science and Technology, Nanjing, Jiangsu, China

modulus of the re-entrant hexagonal structures, which has been regarded as a measurement to validate the finite element analysis. Based on this foundation, the analytical models characterizing mechanical properties of other auxetic structures were explored (Alderson et al. 2010; Gao et al. 2018a). The analytical models for predicting the nonlinear mechanical properties of NPR structures were further developed (Zhang et al. 2018). Hu and Yu (Hu and Yu 2013) and Zhao et al. (Zhao et al. 2018) summarized the deformation modes of the NPR structures under different impact loadings and concluded an empirical formula to distinguish different modes. Explicit formulas of the plateau stress and energy absorption were derived according to the deformation modes of the representative blocks.

Some NPR structures have lower Young's modulus due to their highly porous micro-structure. To overcome this issue, (Fu et al. 2018) revised the common re-entrant hexagonal structures by introducing some beams. The new structures can have higher elastic modulus when keeping the Poisson's ratio negative. Li et al. (2019) did the similar improvement based on the double arrowed structures to enhance the yield stress without sacrificing the negative Poisson's ratio. Lu et al. (2017) proposed two NPR structures (Structure A and Structure B) and evolved structure A into structure B. The analytical models based on the Timoshenko beam theory showed that the combined structures have higher Young's modulus. The geometry of the double arrowed structure was smoothed to double-U structure to reduce the stress concentration and manufacturing challenges (Yang et al. 2019).

More researchers begin to focus on the engineering applications of the NPR structures. An auxetic energy harvester was proposed and studied numerically and experimentally. The contraction in the later direction when compressed in axial direction can improve the efficiency dramatically (Ferguson et al. 2018). The NPR structures were also applied as some vibration parts of which geometry parameters can be designed to control the frequencies (Duc et al. 2017). Wang et al. (2016, 2018b, 2018c) designed a bumper to limit the vehicle suspension displacement based on the double arrowed structures. It is found that the NPR bumper has a better load–displacement curve compared to the traditional one. Various NPR structures were applied as the core of the sandwich to protect from the blast damage (Novak et al. 2019; Lan et al. 2019). Mostly, the NPR structures themselves played roles to absorb energy under impact loading. Gao et al. (Gao et al. 2018b, 2019) studied the effects of the multi-scale parameters on the crashworthiness of three-dimensional NPR structures and optimized a cylindrical NPR structure as a crash box. Inspired by the foam-filled tubes, crash box and bumper system filled with the NPR structure improve the energy absorption performance (Zhou et al. 2016; Wang et al. 2018a). The NPR structures filled in the crash box or bumper system contract when impacted

to increase the stiffness of the whole structure. Simpson and Kazancı (Simpson and Kazancı 2020) investigated the energy absorption of lattice filled structures and found the introduction of the auxetic can increase the energy absorption by about 60%. Baykasoglu et al. (Baykasoğlu et al. 2020), Çetin and Baykasoglu (Cetin and Baykasoğlu 2019) also filled the lattice into the square tube and optimized the new hybrid structure to absorb more energy. Usta et al. (Usta et al. 2018) combined the auxetic structures and trigger tubes to improve the crashworthiness performance. However, this design did not utilize the negative Poisson's ratio. When NPR structures play as fillers, the NPR structures contract more and separate from the crash box, so as to weaken the interaction between the two structures. In contrast, when thin-walled tube plays as inner tube, the NPR structures will contact the inner tube to make them deform more indicating more energy will be absorbed.

In this paper, a cylindrical auxetic structure with inner liner tubes is proposed to overcome the above-mentioned problem. The crashworthiness performances of the novel structure are compared to the single NPR structure, thin-walled tubes and the tube filled with the NPR structures. Then, the parametric analysis of the geometric parameters on the crashworthiness performance are studied thoroughly. Last, a multi-objective optimization algorithm and surrogate modeling technique are employed to optimize the novel structure.

2 Geometric design and material properties

The cylindrical NPR structure (C-NPR) proposed in this paper is based on the double arrowed structure as shown in Fig. 1. The double arrowed unit cell rotates with the center axial and expands in radial direction to form the one layer. Then, the C-NPR structure is assembled by stacking several layers of structures. Since thin-walled tubes have prominent crashworthiness performance, they are introduced in the NPR structures to improve the energy absorption in two ways. Traditionally, NPR structures are filled in the thin-walled tubes, which are similar to the foam-filled thin-walled tubes. The other is the arrangement introduced in this paper, thin-walled tube works as an inner liner tube in the C-NPR structure. Elipe and Lantada (2012) proved that the re-entrant hexagonal and double arrowed honeycombs have the largest effective Young's modulus, which is at least 10 times the other types. The re-entrant hexagonal structures are easy to buckle and therefore the double arrowed structure is selected.

The C-NPR structure has the following geometries: number of layers nl , number of cells in one layer nc , inner radius r_i , outer radius r_o , the thickness of the long beams and short beams composed of the unit cell t_l and

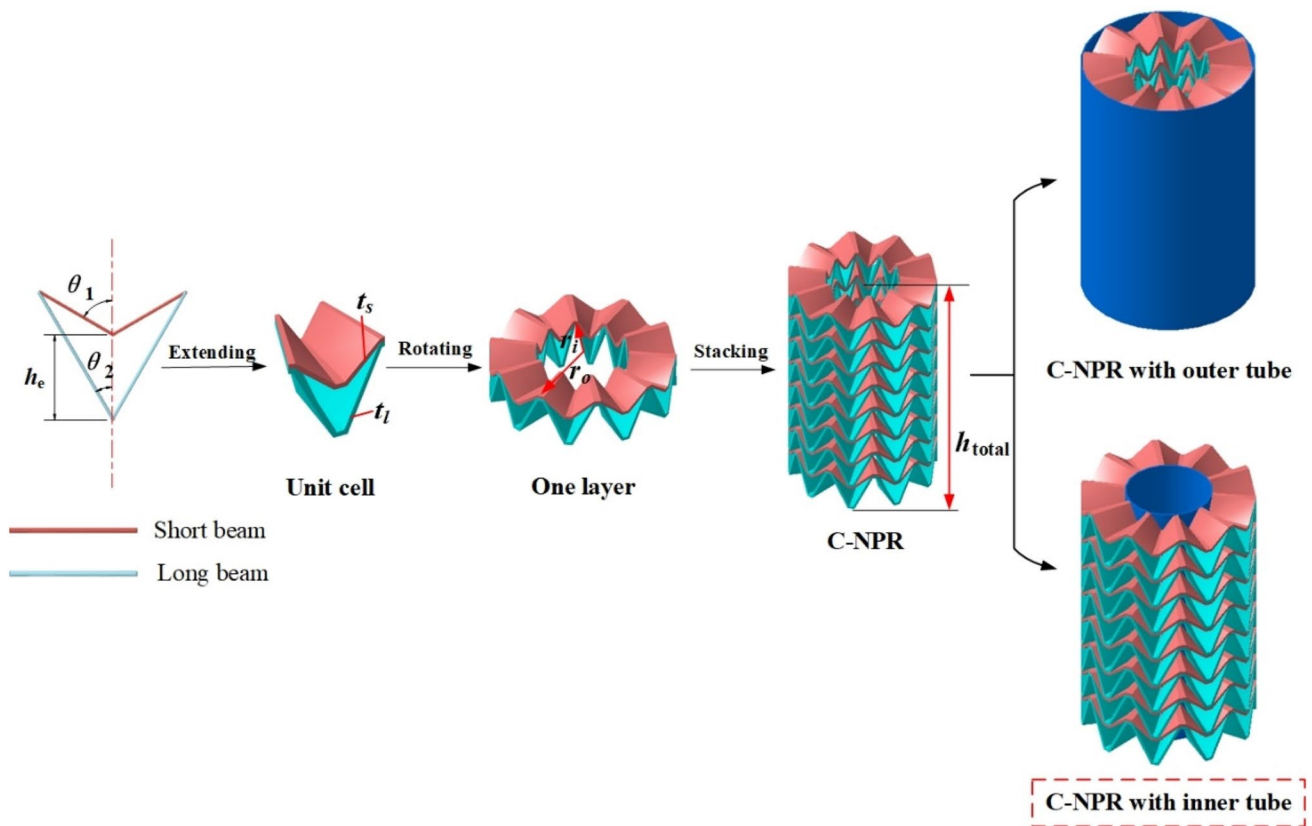


Fig. 1 Geometric description of the cylindrical NPR structures and thin-walled tubes

t_s , effective height of the unit cell h_e and the total height h_{total} . It is noticed that nl and nc have to be integer and h_{total} is fixed as 250 mm referring to the geometric size of crash box. The radius of the thin-walled tubes above-mentioned are determined according to the outer radius and inner radius of C-NPR structures. The thickness of the tube is denoted as t_t .

The C-NPR adopt the printing material AlSi10Mg. To obtain the material properties, a tensile specimen is manufactured with 3D printing technique, which is applied to fabricate the prototype later (Fig. 2a). The ASTM E8 Standard Test is performed to obtain the stress–strain curve of printing material as shown in Fig. 2b. The initial and ultimate stress are 228 and 326 MPa. Thin-walled tube adopts the material AA6061 T4 with the Poisson's ratio $\nu = 0.33$, Young's modulus $E = 68$ GPa, density $\rho_s = 2700\text{kg/m}^3$, initial yield stress $\sigma_y = 80$ MPa, ultimate stress $\sigma_u = 173$ MPa and the power law exponent $n = 0.23$. The stress–strain curve is illustrated in Fig. 2c. The effect of the strain rate under dynamic loading is sufficiently small to be ignored (Nikkhah et al. 2019).

3 Modeling and validation

3.1 Finite element model

To study the crashworthiness performance of the C-NPR structures with outer/inner tubes under impact loading, the software LS-DYNA is employed. As shown in Fig. 3, the bottom of the C-NPR structure is fully fixed, while the top is impacted by a rigid wall with 10 m/s, which is the impact velocity used to evaluate the crashworthiness performance of the thin-walled tubes. C-NPR structures and thin-walled tubes are simulated with the Belytschko-Lin-Tsay shell elements with five integration points through the thickness. The shell elements are placed on the mid surface. Since the initial penetration is very small, the function “*CONTROL_CONTACT” is employed to deal with this to ignore the effect of the initial contact. Figure 4 illustrates the convergence test of the meshing size and it is found that the energy-displacement curve has been stable when meshing size is set as 2 mm. The basic meshing size

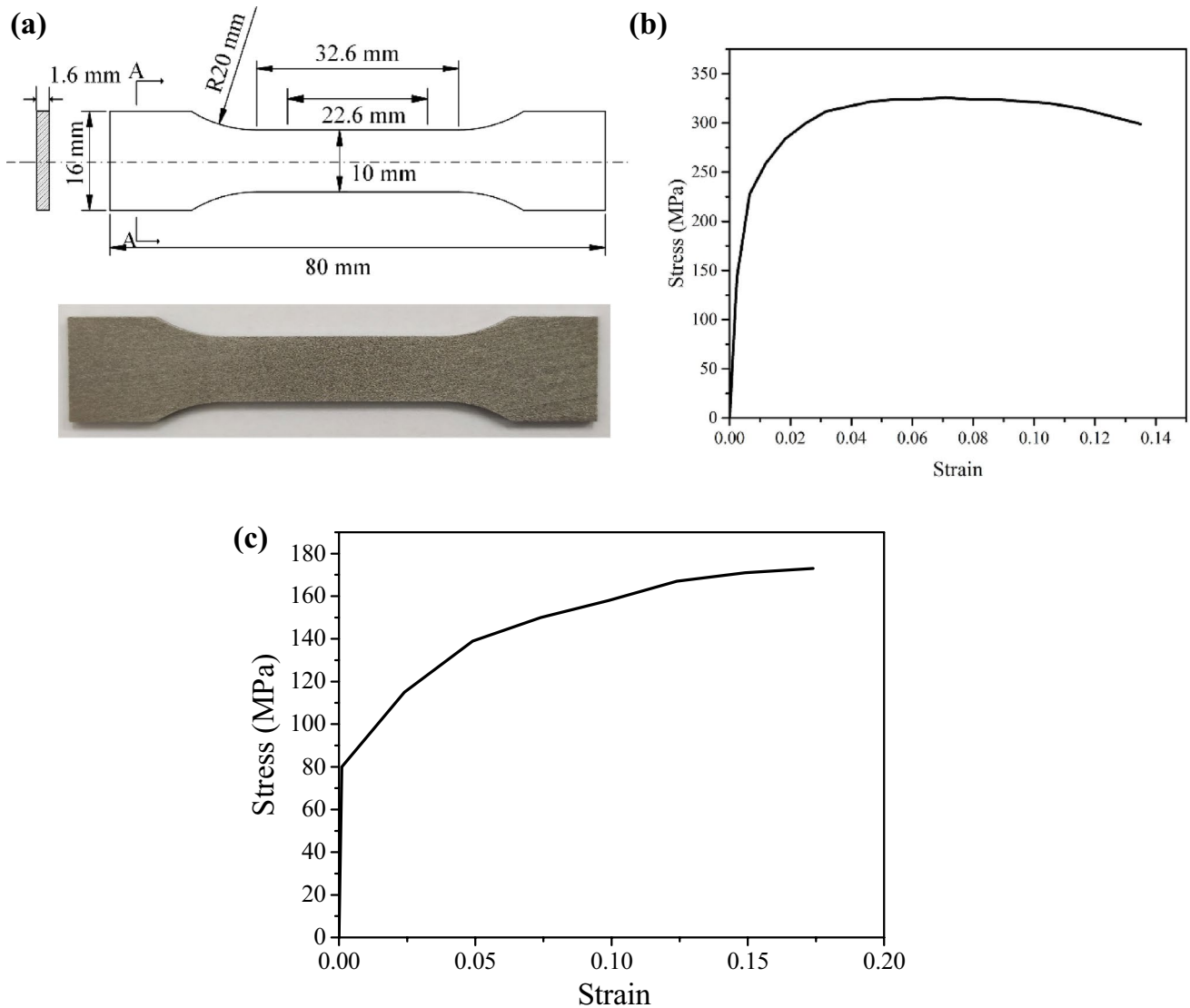


Fig. 2 Tensile specimen (a), the stress–strain curves for AlSi10Mg (b) and AA6061 T4 (c)

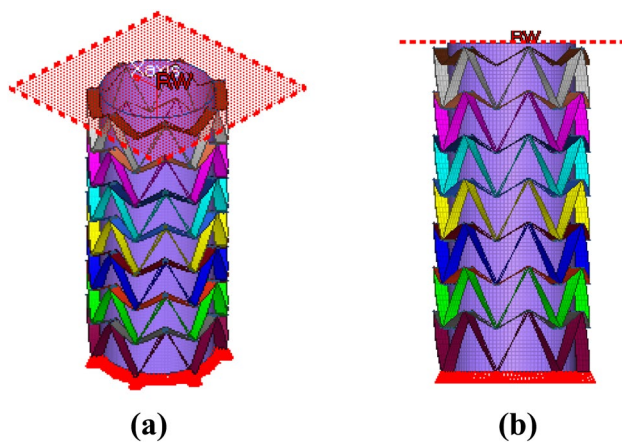


Fig. 3 Finite element model of C-NPR-IT under axial impact loading. **a** Isometric view; **b** Front view

in the following simulations is set as 2 mm. To avoid the self-interpenetration of the structures, ‘Automatic single surface’ algorithm is employed for each layer of structure and the thin-walled tubes. ‘Automatic surface to surface’ is used to simulate the contact between different layers of structures, the thin-walled tubes and C-NPR structure. The contact between the rigid wall and C-NPR structure with thin-walled tubes is simulated with the ‘Automatic node to surface’ algorithm. All the friction coefficients are set as 0.3 (Gao et al. 2018b). Regarding the material modeling, #24 material in LS-DYNA has been proved to have a good prediction (Huang and Xu 2019).

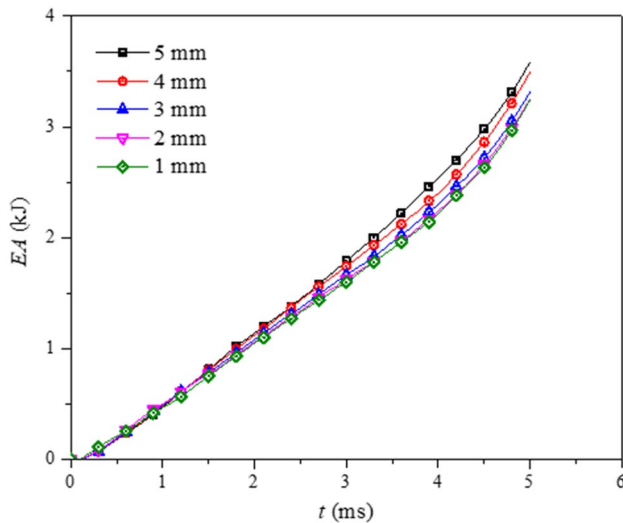


Fig. 4 Convergence test of the meshing size

3.2 Crashworthiness indicators

There are some common indicators used to characterize the crashworthiness performance of the thin-walled tubes and auxetic structures, such as energy absorption (EA), specific energy absorption (SEA), peak crushing force (PCF). The indicators are defined as follows:

Energy absorption (EA) characterizes the energy absorption capabilities of the C-NPR with inner tube during the compression and it is represented:

$$EA = \int_0^{\delta} F(s) ds \quad (1)$$

where $F(s)$ is the instantaneous crushing force in the impact direction, δ is the stroke distance, which is taken as the 80% of the total height of the C-NPR.

Considering the effect of the mass of the C-NPR in the design, SEA is proposed to represent the energy absorption per mass:

$$SEA = \frac{EA}{M} \quad (2)$$

where M is the total mass of the whole structure.

Peak crushing force (PCF) is the largest crushing force during the crushing and represented as follows:

$$PCF = \max[F(s)] \quad (3)$$

In the evaluation of the passive safety of the vehicles in the collision, PCF is critical because it determines the injury of the occupants (Wu et al. 2016; Qiu et al. 2016; Gao et al. 2016).

3.3 Experimental validation

A C-NPR prototype was manufactured by the equipment FS271M with a $275 \times 275 \times 320$ mm building platform and an up to 500 W continuous Yb: YAG fiber laser as shown in Fig. 5. It was fabricated from a pre-alloyed AlSi10Mg powder with a particle size in the range of 15–30 μm . The scanning speed was about 1 m/s and the spot size of the laser was about 120 μm in diameter. Layer thickness prior to melting was 60 μm . Thin-walled tube was bought from the factory directly. The geometric parameters of the prototype are summarized in Table 1. The material herein is the aluminum alloy with the same material properties in the last section. Due to the limitation of the experimental cost and condition, the size of the prototype is designed to be small and the quasi-static compression test is conducted instead of the impact test. The comparisons between the stress–strain curves of the experiments and numerical models can be used to validate the model. In the quasi-static compression test, the prototype is placed on the platform of the universal testing machine INSTRON3380. The range of force and displacement for this machine can reach 100 kN and 1323 mm. The measuring error of the force and displacement can be limited under 0.5% and the sampling frequency is set as 2 Hz in the experiment. Both the compression speed is set as 10 mm/min in the experiments and simulations. Figure 5c compares the force–displacement curves of experiments and simulation and it can be found that they agree reasonably, which indicates the established finite element model can predict the mechanical properties of the C-NPR-IT structure accurately. The errors of peak crushing force and energy absorption are only 3.1 and 3.7%, respectively. There is a discrepancy in the force–displacement of FEA and experiment after the first peak due to the defect of the prototype caused by the manufacture process. As shown in Figs. 5d, the deformation patterns in experiments and finite element model are similar. The differences between the numerical and experimental results are mainly caused in two ways: (a) The manufacturing errors; (b) the ignorance of fracture in the finite element model (Fig. 6).

4 Results and discussion

4.1 Energy absorptions of different configurations

The crashworthiness performance of the single C-NPR (S-C-NPR), single outer/inner thin-walled tube (S-OT/IT), C-NPR structure with outer tube (C-NPR-OT) and C-NPR structures with inner tube (C-NPR-IT) under axial impact loading ($v = 10$ m/s) are compared. Figure 7 compares the deformation modes of the S-C-NPR, C-NPR-OT and C-NPR-IT under several specific compression displacement, 40, 80, and

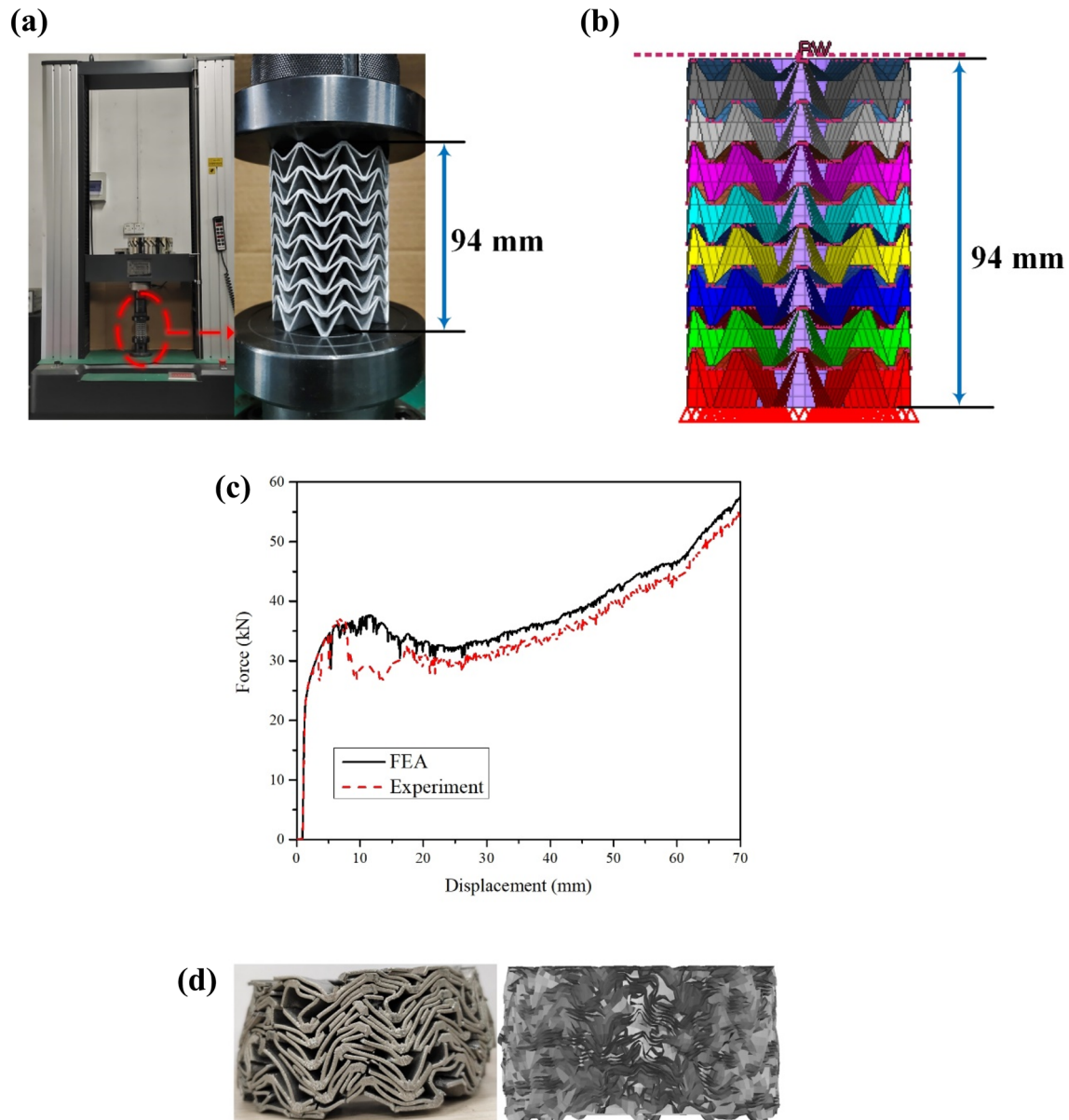


Fig. 5 Quasi-static compression test of the NPR structure with inner tubes. **a** Experiment, **b** Numerical simulation, **c** Force–displacement curves, **d** Deformation patterns

120 mm. It is found that S-C-NPR contracts inward because of the negative Poisson's ratio. The deformation modes can enhance the stiffness of the structure to absorb more energy. However, the stiffness of the structure is small. Thin-walled structures are introduced into the S-C-NPR to address the issue. C-NPR-OT structure places the C-NPR as a filler of the structure like the foam-filled thin-walled tubes. It aims to increase the energy absorbed by introducing the interaction between the thin-walled tube and C-NPR. NPR structure can also contract during the deformation process. However, the contraction part of NPR structure cannot contact the thin-walled tube effectively. Therefore, the introduction

of the auxetic filler plays a small role on the improvement of energy absorption. Actually, when the C-NPR contracts inward in the middle of part, the end of the structure will deform outward slightly and contact to the outer thin-walled tube, which is the main cause of the improvement on the energy absorption performance. Regarding the introduction of the filler of thin-walled tubes, a lattice structure with positive Poisson's ratio is preferred.

The force–displacement curves of different structures are compared in Fig. 6. There is a peak crushing force followed by a steady crushing force. It is found that C-NPR-IT structure has the largest crushing force during the deformation

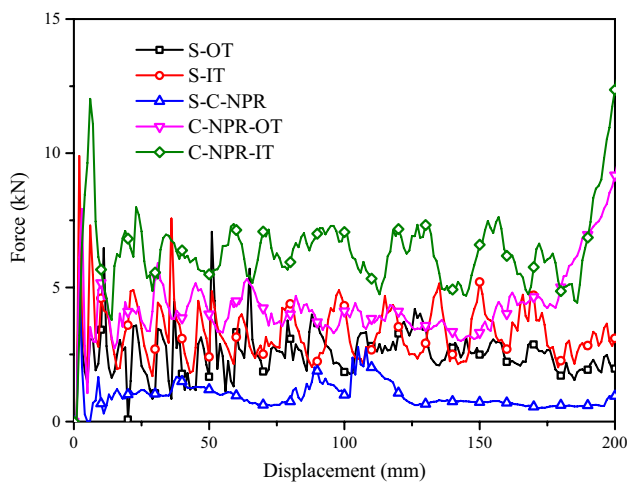


Fig. 6 Force–displacement curves of different structures

patterns. S-OT, S-IT and S-C-NPR structures have lower crushing forces, and the summation of the S-IT and S-C-NPR is still lower than that of C-NPR-IT.

As shown in Table 2, we compare the energy absorption of the C-NPR-OT structure and the S-C-NPR and S-OT structures. The deformation distance is defined as 200 mm. It is found that the corresponding part can absorb more energy than the single ones. The C-NPR in C-NPR-OT can absorb more energy by 21.4% and the OT in C-NPR-OT structure can increase the energy absorption by 11.5%. Totally, the C-NPR-OT structure improves the energy absorption performance by 14%. However, the contraction part can hardly contact the thin-walled tube to do any contribution. Hence, the improvement is not much satisfied.

To sufficiently utilize the contraction of the NPR structure, C-NPR-IT structure is proposed in which the thin-walled tube works as a linear tube. As shown in Fig. 7, C-NPR cannot contract inward due to the support of the inner tube. The interaction between the tube and NPR structure in C-NPR-IT structure is much more than that in the C-NPR-OT structure. In addition, the interaction can make thin-walled tube to generate more folding parts, which determine the energy absorption. C-NPR structure can deform more sufficiently to produce more hinges. All of these contribute to the improvement of the energy absorption of C-NPR-IT structure as shown in Table 2. The unique design even doubles the energy absorption of the C-NPR in C-NPR-IT structure. The energy absorption of the whole structure and the corresponding single IT structure increase by 48.3 and 22%, respectively. Considering the effects of the mass on

the energy absorption, the mass of C-NPR-OT and C-NPR-IT structures are designed to be the same. Regarding the specific configuration in Table 2, the C-NPR-IT structure can absorb about 400 J more than C-NPR-OT by around 50%. It is found that the energy dissipated due to the interaction is close to the sum of the energy absorbed by single NPR structure and single thin-walled tube. This indicates that the novel C-NPR-IT structure proposed has great potential as energy absorbers under axial impact loading. Considering the effects of the weight, the SEAs of the pure thin-walled tube, C-NPR-OT and C-NPR-IT are 2.31, 1.94 and 2.87 kJ/kg. It is noted that the C-NPR-IT has higher SEA indicating the C-NPR-IT structure is a better energy absorber.

4.2 Parametric analysis

The energy absorption of C-NPR-IT structure is consisted of three parts: energy absorption of C-NPR structure, energy absorption of IT structure and the interaction between them. Therefore, the energy absorption performances are affected by the geometric parameters of the C-NPR and IT structures. These geometric parameters can not only affect the energy absorption of considering structures themselves but also the interaction. Herein, effects of such geometries as nl , nc , r_i and the thickness of beams for NPR structure and tube on crashworthiness performance are analyzed. These parameters have been studied to have great effects on the crashworthiness performance on the single NPR structures and single thin-walled tubes (Qiu et al. 2018; Gao et al. 2018b). *SEA* and *PCF* are utilized to characterize the crashworthiness performance. A basic model with $nl=7$, $nc=7$, $t_s=1\text{ mm}$, $t_l=1\text{ mm}$, $t_i=0.5\text{ mm}$, $r_o=60\text{ mm}$, $r_i=50\text{ mm}$ and $h_{\text{total}}=250\text{ mm}$ is established to conduct the parametric analysis. In the parametric analysis, except for the parameter studied, the other parameters are kept the same as the basic model.

4.2.1 Effects of number of layers nl

The number of layers nl can be varied to study the crashworthiness performance of the C-NPR-IT structure. To keep the total height h_{total} unchanged, two strategies are proposed. One is the short beam angle θ_1 is constant as 60° , long beam angle θ_2 is adjustable. The other one is opposite: θ_2 equals 25° and θ_1 is adjustable. The force–displacement, *PCF* and *SEA* of different configurations are illustrated in Fig. 8. It is found that there is a great peak force at displacement of about 5 mm. Then the force drops

Table 1 Geometric parameters of the manufactured prototype

Parameters	nl	nc	r_i/mm	r_o/mm	h_e/mm	t_l/mm	t_s/mm	t_i/mm	$h_{\text{total}}/\text{mm}$
Values	8	10	15	30	11	1	1	0.5	94

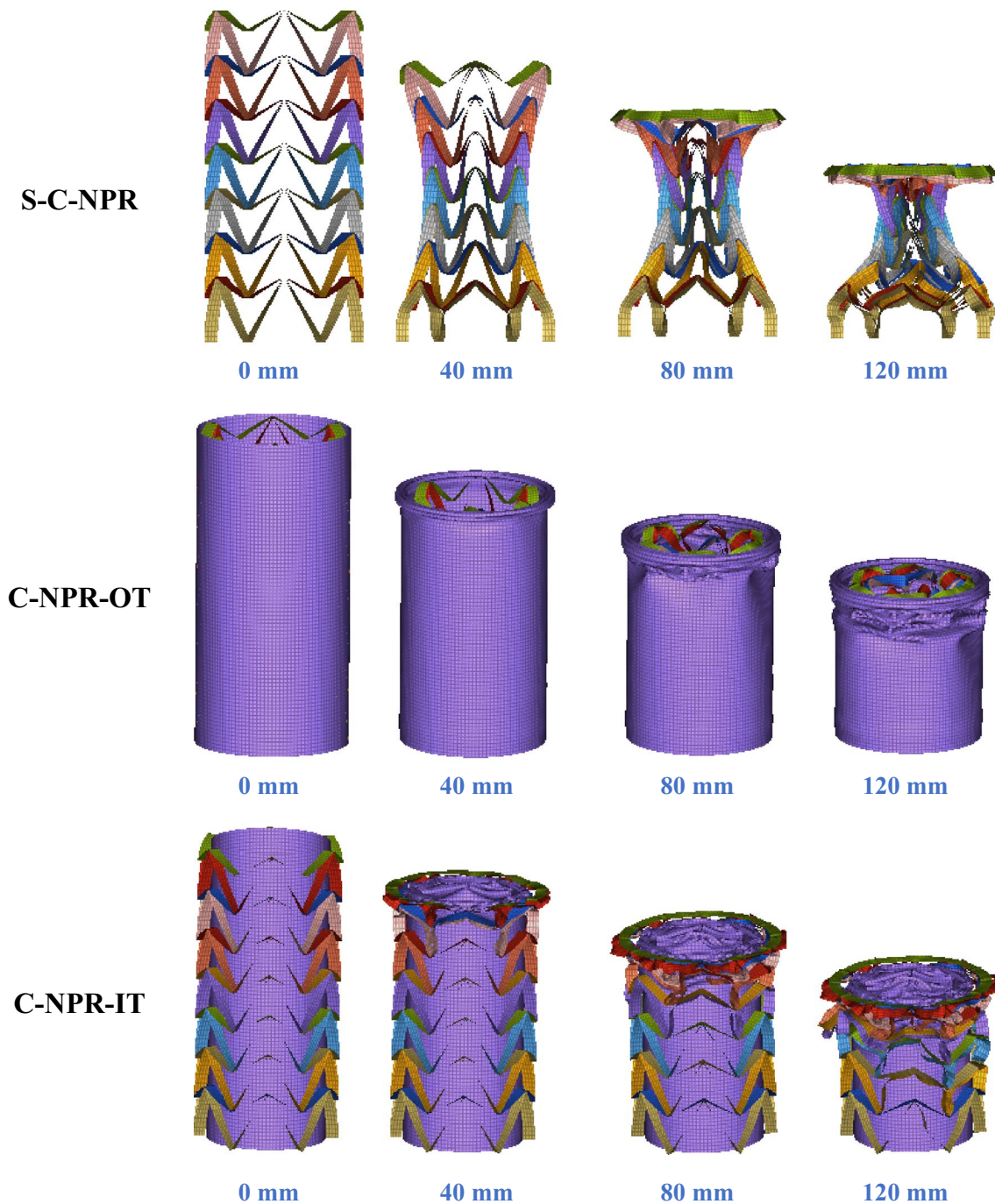


Fig. 7 Deformation modes of different structures under axial impact loading ($v = 10$ m/s)

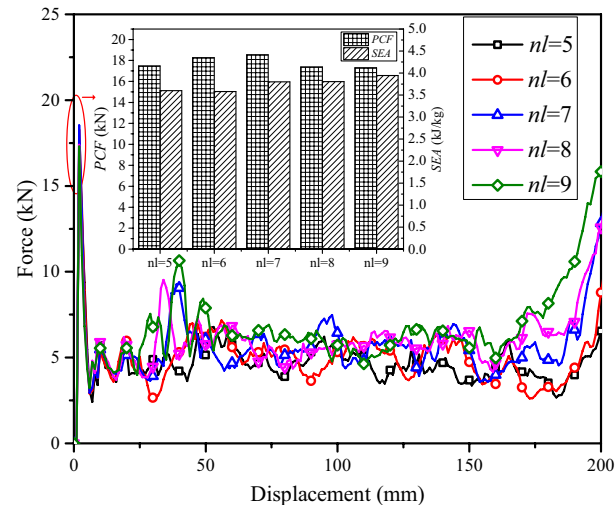
dramatically to a steady value, which is corresponding to the plateau stress of the C-NPR-IT structure. The ups and downs are caused by the deformation modes of the C-NPR and thin-walled tubes. As shown in Fig. 7, the C-NPR structure deforms layer by layer and the thin-walled tube collapses in a regular pattern. In each deformed unit, the stiffness of the structures is varied. With the increase of the impact displacement, C-NPR structure enters into

the densification regions, which make the impact force increase remarkably.

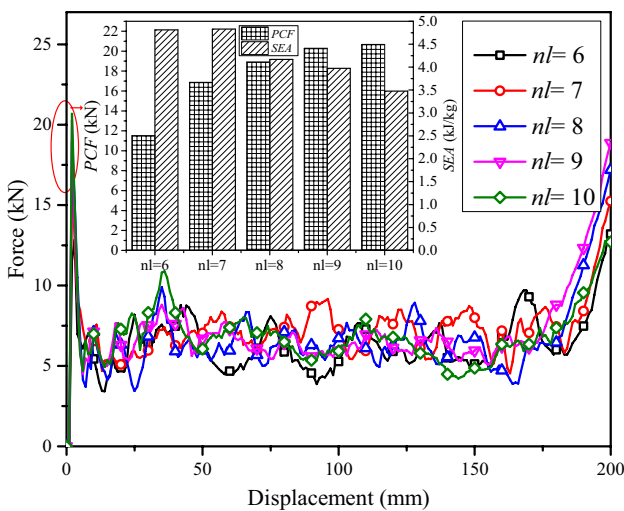
Regarding the *PCF* and *SEA* of C-NPR-IT structure with varying nl , there is no obvious effect when θ_1 is constant, while the effect is remarkable when θ_2 is constant. The long beam is closer to the vertical position than the short beam, $\theta_2 < \theta_1$. To keep the total height h_{total} constant, the change of θ_2 is always larger than θ_1 . Therefore, the effect of the nl by

Table 2 Comparisons of the energy absorption of different structures

	Energy Absorption (J)		Increment (%)
	S-C-NPR + S-OT	C-NPR-OT	
S-C-NPR	180.322	218.909	21.4
S-OT	515.806	574.915	11.5
Total	696.128	793.824	14
S-C-NPR	180.322	387.563	114.9
S-IT	647.353	789.957	22
Total	827.675	1177.52	48.3



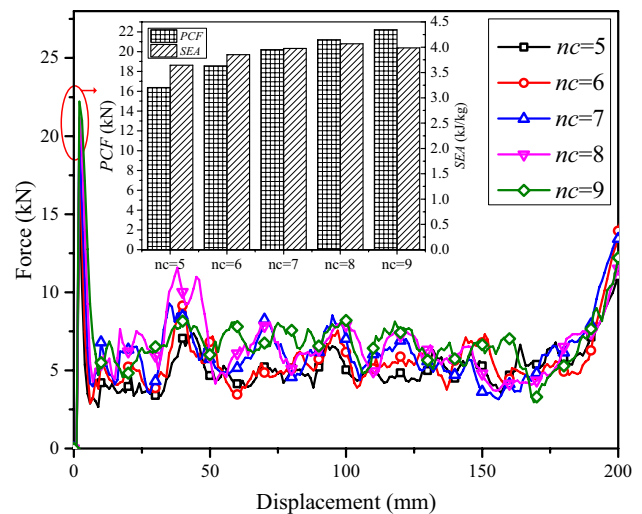
(a)



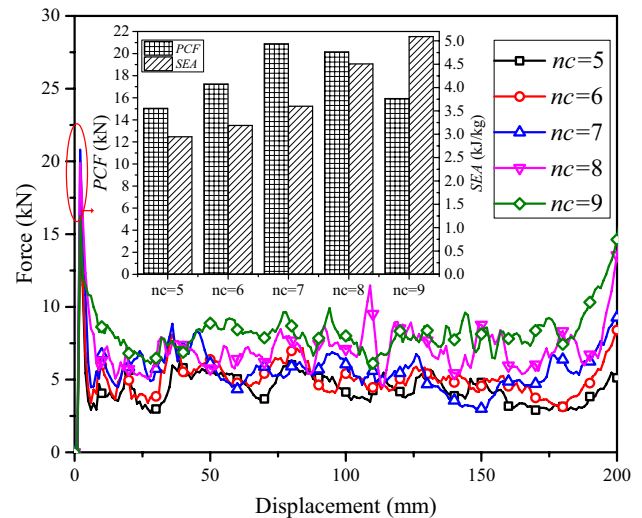
(b)

Fig. 8 Effects of nl on crashworthiness performance (a) $\theta_1 = 60^\circ$; (b) $\theta_2 = 25^\circ$

adjusting θ_1 is more obvious indicating that θ_1 should attract more attentions in the design.



(a)



(b)

Fig. 9 Effects of nc on crashworthiness performance (a) $\theta_1 = 60^\circ$; (b) $\theta_2 = 25^\circ$

In the second scenario as shown in Fig. 8b, while nl increases, θ_1 and the effective height of the unit cell drop to make the C-NPR structure enter into densification region earlier to absorb more energy. Meanwhile, the mass of the structure also increases to make a negative effect on the SEA. Comprehensively, the C-NPR-IT with $nl = 6, 7$ has larger SEA. There is a sudden drop on SEA when nl changes from 7 to 8. It is essential to avoid the design that nl is less than the critical number to guarantee the SEA. PCF grows with the increase of nl and the growth rate is becoming slower gradually. This is because the stiffness of the C-NPR will increase as nl grows when θ_2 is constant. Also, the growth rate of the stiffness is smaller when nl is large. There is a strong nonlinear effect of nl on the crashworthiness performance considering both SEA and PCF. In designing the

C-NPR-IT structure as an energy absorber, it is critical to choose a suitable nl .

4.2.2 Effects of number of cells nc

The number of cells in one layer nc also has great effects on the crashworthiness performance (Fig. 9). Similarly, total height h_{total} is kept the same by adjusting θ_1 and θ_2 , respectively. Different from the previous section, the changes of nc by adjusting θ_2 have prominent effects on the crashworthiness performance. Since the number of cells nc increases, the stiffness of each layer grows to cause the larger PCF . SEA also increases synchronously except that SEA of the C-NPR-IT with $nc=9$ decreases slightly because of too large mass. When $\theta_2=25^\circ$, with the increase of nc , the mass will reduce instead that benefits the SEA significantly. The SEA of the C-NPR-IT with $nc=9$ is almost twice of the one with $nc=5$. It is more satisfied that their PCF are still on the same level. With the increase of nc , PCF will grow first and then drop. When $\theta_2=25^\circ$, with the increase of the nc , the stiffness of cell will increase, while the material composed of the whole structure reduces making the whole structure softer. At the first stage, the effect of the increase of the cells dominates to cause larger PCF . When $nc=9$, the effect of the increase of the cell is dominated to reduce the PCF . The C-NPR-IT with $nc=7$ has the highest PCF , which indicates this configuration should be avoided in the design. It is found that the effects of nc on SEA are more significant on the PCF . Therefore, if we want to improve SEA without increasing PCF much, it is a good option to increase the number of cells.

4.2.3 Effects of thickness

Thicknesses of the long and short beams of single cubic and cylindrical NPR structures have been studied to determine the deformation modes, which are directly related to the energy absorption (Gao et al. 2018b, 2019). It is also necessary to study the effect of the beam thickness and tube thickness on the crashworthiness performance of C-NPR-IT structure to provide guidance to the designers.

Thickness of beams, t_s and t_l , vary from 0.5 to 2.5 mm at an interval of 0.5 mm to study the effects on the crashworthiness performance. As shown in Fig. 10a, b, the effects of the beam thickness on crashworthiness performance are determined by relative values of the short and long beam thickness instead of the single thickness. When $t_s=t_l$, the stiffness of short beam is higher according to the geometry configuration and Euler beam theory. Even though the short beam with $t_s=0.5$ mm is still stiffer than the long beam with $t_l=1$ mm. In other words, all structures in Fig. 10a have softer long beams, which will buckle first in the initial impact procedure. Therefore, t_s has slight effect on PCF

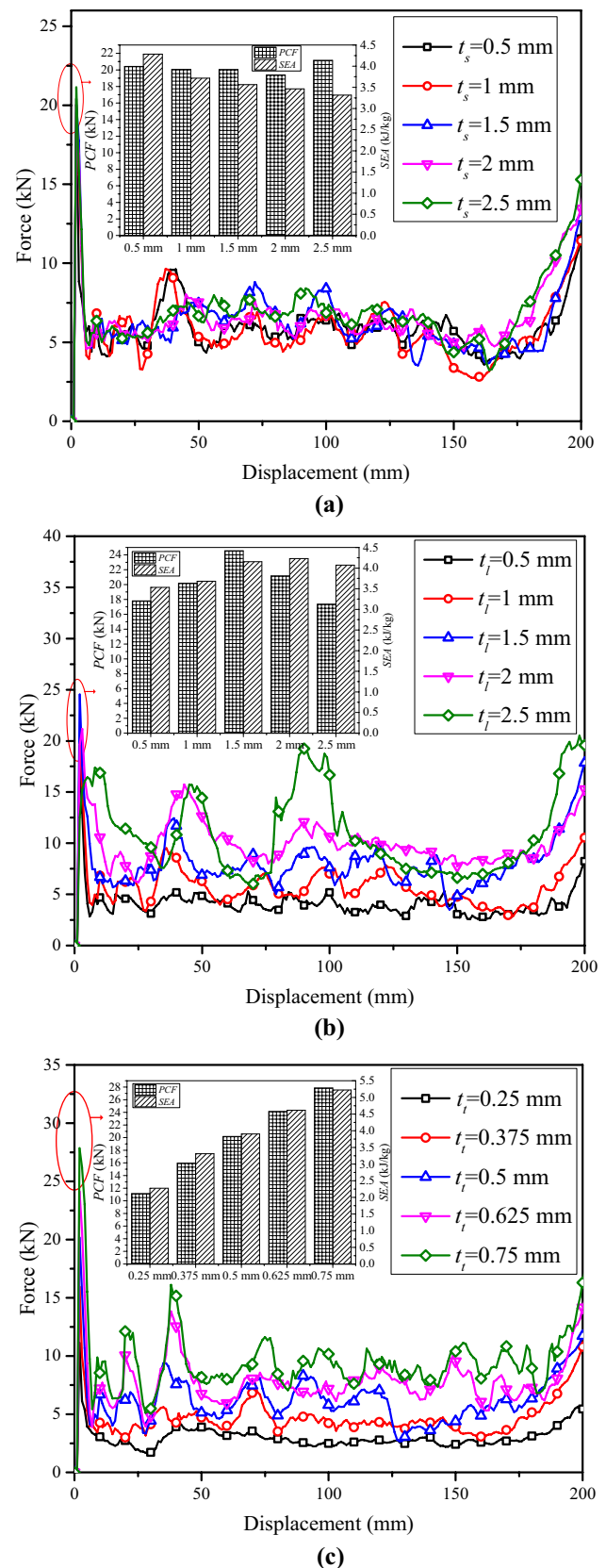


Fig. 10 Effects of thicknesses on crashworthiness performance **a** thickness of short beam t_s ; **b** thickness of long beam t_l ; **c** thickness of tube t_t

when t_l is constant in Fig. 10a. On the contrary, the effects of t_l are prominent as shown in Fig. 10b where $t_s=1$ mm. When $t_l \leq 1.5$ mm, PCF grows with the increase of t_l since the stiffness of long beam is increased. However, once $t_l > 1.5$ mm, PCF drops dramatically because the short beam will buckle first instead of the long beam.

Besides, t_s and t_l have the opposite effects on SEA . The increase of t_s has a negative effect on SEA because of the increase of the mass. However, the enhancement of stiffness of long beam can contribute to the SEA than the negative effects of the mass. When $t_l \geq 1.5$ mm, the positive and negative work cancels out to make the SEA steady on a high level. It can be concluded that the larger t_l is preferred to achieve the higher SEA and lower PCF .

It is evident that the increases of the t_l have synchronous effects on the SEA and PCF as shown in Fig. 10c. PCF and SEA increase significantly when t_l grows. With the increase of t_l , the stiffness of the thin-walled tube is larger to support the contraction of the NPR structures, indicating the interaction will be enhanced further. However, the increases of the stiffness of the tubes also cause the overlarge PCF . It is an effective method to maximum the SEA by designing larger t_l . However, in the engineering design, there is a limitation to the PCF , such as crash box where $PCF \leq 80$ kN is required. Too large PCF means great acceleration speed to cause passengers injury in the vehicles. Therefore, it is essential to design the parameters of C-NPT-IT structure reasonably considering the trade-off between the SEA and PCF .

4.2.4 Effects of inner radius r_i

The effects of the inner radius of r_i on the crashworthiness indicators PCF and SEA are illustrated in Fig. 11. As

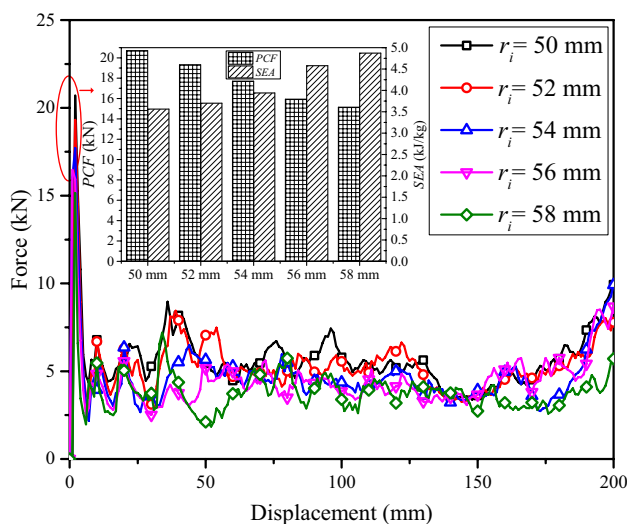


Fig. 11 Effects of the inner radius r_i on crashworthiness performance

we know, when r_i increases, the mass of NPR structure in C-NPR-IT will reduce, while the mass of thin-walled tube will increase. In the basic model, the total weight is reduced because t_l is only the half of $t_s(t_l)$. Therefore, the increase of the r_i causes the increment of the SEA and decrease of PCF which are both benefit for the crashworthiness performance. According to the basic model, small r_i is preferred. Regarding the tube thickness and radius, there is a coupling effect on the energy absorption performance (Abramowicz and Jones 1986). Once the geometry configurations of the basic NPR structure and thin-walled tubes change, there will be another statement. The optimal r_i will be discussed in the next section considering more designs.

The force–displacement curves of C-NPR-IT with smaller inner radius ($r_i = 40, 30, 20, 10, 5$ mm) are also illustrated in Fig. 12. It can be found that the peak crushing forces grow dramatically. The peak crushing force of C-NPR-IT with $r_i = 5$ mm is more than ten times of that of the C-NPR-IT with $r_i = 50$ mm in Fig. 12. Also, at the densification state, the crushing force will be larger than initial peak crushing force. Then the energy absorption cannot be qualified using the 80% stroking distance. It is noticeable that the mass of the structures grows dramatically from 0.3212 kg ($r_i = 50$ mm) to 1.181 kg ($r_i = 5$ mm), which is deviating from lightweight design. Therefore, a narrow range of the inner radius is selected in this paper.

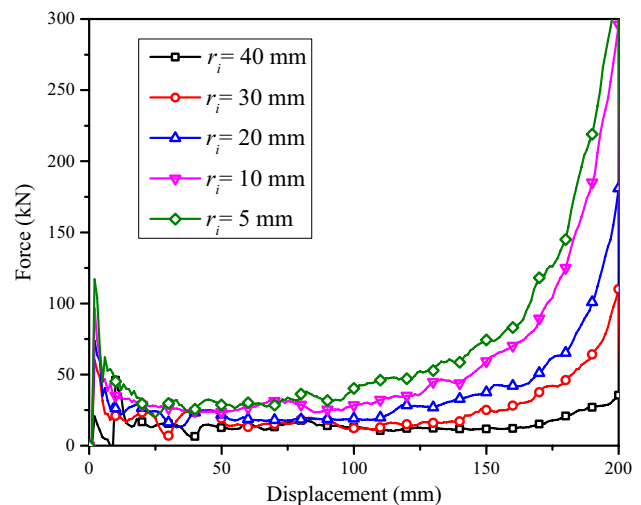


Fig. 12 Force–displacement curves for NPR-IT with different inner radius

5 Multi-objective optimization

5.1 Optimization problem

Since geometric parameters of C-NPR-IT structure have great nonlinear and coupling effects on the crashworthiness performance, it is hard to design the optimal structure directly. A multi-objective optimization scheme employing a penalty function is introduced to solve the problem (Kitayama et al. 2006). It is noticeable that nl and nc represent the number of layers and cells of C-NPR, which are required to be integer. Since only when $\theta_1 > \theta_2$, the structure designed has the negative Poisson's ratio. In other words, the effective height h_e should be larger than zero. According to the designing experience, the ranges of the parameters are set and h_{total} and r_o are fixed as 250 and 60 mm, respectively. SEA and PCF are the mostly concerned objectives in the real engineering design. The higher SEA and lower PCF are preferred (Zhang et al. 2012; Qi et al. 2012; Li et al. 2014; An et al. 2015; Pirmohammad and Esmaeili-Marzdashti 2019). Then, the optimization problem considering number of layers (nl), number of cells (nc), thickness of beams and tubes (t_l, t_s, t_t), inner radius (r_i), mass and effective height (h_e) is described as follows:

$$\begin{aligned} \min : & \{ -EA, PCF \} \\ \text{s.t.} & \quad 4 \leq nl, nc \leq 12 \ \& \ nl, nc \text{ are integer} \\ & \quad 0.4 \text{ mm} \leq t_l, t_s, t_t \leq 3 \text{ mm} \\ & \quad 40 \text{ mm} \leq r_i \leq 58 \text{ mm} \\ & \quad 15 \text{ mm} \leq h_e \leq 40 \text{ mm} \\ & \quad 0.3 \text{ kg} \leq \text{mass} \leq 0.5 \text{ kg} \\ & \quad h_{\text{total}} = h_e nl + (t_s + t_l)nl/2 = 250 \text{ mm} \end{aligned} \quad (4)$$

5.2 Surrogate modeling

Since the explicit formulas of SEA and PCF are hard to achieve and the numerical simulation is time-consuming, a surrogate modeling technique is employed to characterize the relationship between the designed parameters and optimization objectives. The technique is based on the training points from the simulation results chosen with the sampling method. An optimal Latin Hypercube sampling (OLHS) including the enhanced stochastic evolutionary (ESE) algorithm was proposed to efficiently construct medium to large-sized design of experiments (Jin et al. 2005). Shang et al. (2020) studied different kinds of OLHS to find that the OLHS with ESE algorithm performs best when design parameters are less than 10. Then, a surrogate model based on Radial Basis Function (RBF) network is established based on the training points. The accuracy of the RBF model

needs to be validated. To guarantee the accuracy of the RBF model, 200 sampling points are generated for establishing the RBF model and 30 extra points are generated for the model validation. The errors of the validation points are less than 5%, which can be allowed in the engineering field. The error of the RBF model can be quantified with indicator RE ,

$$RE = \left| \frac{y_i - \hat{y}_i}{y_i} \right| \quad (5)$$

where y_i and \hat{y}_i are the crashworthiness responses of the finite element simulation and RBF models for point i . Meanwhile, the R^2 is up to 0.96 implying the RBF model is accurate enough.

$$R^2 = 1 - \frac{\sum_{i=1}^q (y_i - \hat{y}_i)^2}{\sum_{i=1}^q (y_i - \bar{y}_i)^2} \quad (6)$$

where \bar{y}_i is the mean of y_i and q is the number of confirmation sampling points.

To eliminate the effects of the units in optimization objectives, the EA and PCF are transformed into the dimensionless form according to Eq. (7).

$$X' = \frac{X - X_{\min}}{X_{\max} - X_{\min}} \quad (7)$$

where X' represent the dimensionless value of EA and PCF , X_{\min} and X_{\max} are the minimum and maximum values of EA and PCF , X is the original value of EA and PCF .

5.3 Multi-objective optimization

Multi-objective particle swarm optimization (MOPSO) algorithm is implemented to solve the optimization problem, which including the continuous and discrete design parameters. The MOPSO optimization based on the particle swarm optimization (PSO) algorithm using a dynamic neighborhood to find local optima (Lbest) for each particle in bi-objective optimization problems. The algorithm searches for Lbest that is used as the global best (Gbest) in the PSO algorithm by finding the nearest particles as the neighbors of the current particle. The particle best (Pbest) is the best position in a particle's history when a new position dominates the current position. The optimization procedures are illustrated thoroughly in Fig. 13.

Table 3 summarizes the MOPSO algorithm parameters, which can guarantee the convergence speed and optimization quality in the crashworthiness optimization problems (Yin et al. 2014). Since the objective EA and PCF are conflicting each other, the optimization results are the Pareto frontiers represented by the squares as shown in Fig. 14. The C-NPR-IT structures in the top-left corner have the largest EA along with the unaccepted PCF . In the lower right corner, the

Fig. 13 Flowchart of optimization procedure for C-NPR-IT structure

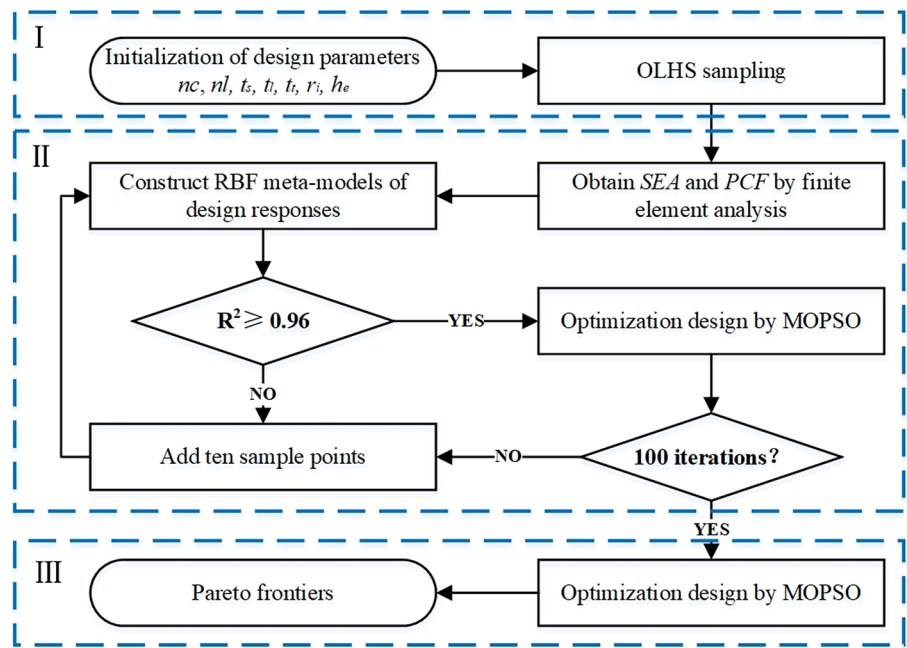


Table 3 MOPSO algorithm parameters

MOPSO parameter	Value
Population size	100
External archive size	100
Inertial weight	0.73
Personal learning coefficient	1.50
Global learning coefficient	1.50

Table 4 Comparisons between the basic and optimal C-NPR-IT structures

	Basic design	Optimized design	Change
<i>nl</i>	7	6	- 1
<i>nc</i>	7	8	+ 1
<i>t_s</i> (mm)	1	1.71	+0.71
<i>t_i</i> (mm)	1	0.76	- 0.24
<i>t_r</i> (mm)	0.5	1.7	+ 1.2
<i>r_i</i> (mm)	50	56	+ 6
<i>h_e</i> (mm)	32.84	38.49	+ 5.65
Mass (kg)	0.3237	0.4916	+ 0.1679
<i>EA</i> (kJ)			
FEA	1.28	4.95	+ 3.67
RBF	1.33	5.02	-
Error (%)	3.4	1.6	-
<i>PCF</i> (kN)			
FEA	20.19	65.91	+ 45.72
RBF	19.36	68.23	-
Error (%)	4.1	3.5	-

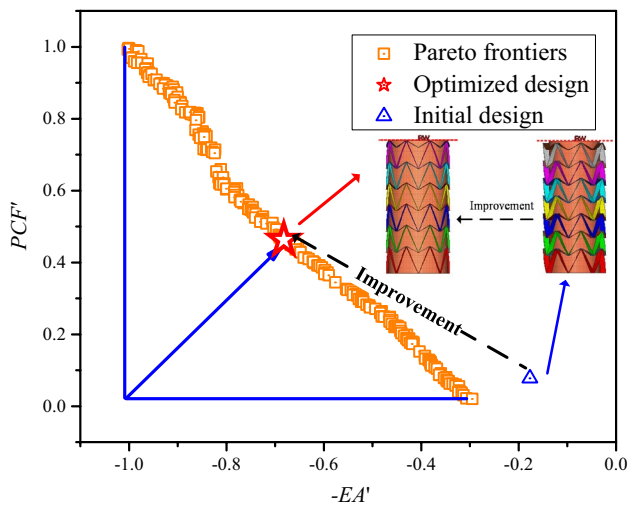


Fig. 14 Pareto frontiers for the C-NPR-IT structures

C-NPR-IT structures have the minimum *PCF*, while the *EA* is too low. To decide the most satisfactory overall solution from the Pareto front, a knee point was determined and represented by the star in Fig. 14, which indicated the minimum distance from the knee point to the utopia point (Sun et al. 2011). Compared to the initial design (up-triangle), the star is on the top-left of up-triangle which means the optimized structure has higher *EA* and *PCF*. The details of geometric parameters and crashworthiness performance for the initial

and optimized designs are summarized in Table 4. In the optimal structures, NPR structures absorb 0.62 kJ and thin-walled tubes absorb 2.75 kJ indicating they are both important to the energy absorption of the whole structure. The accuracy of the RBF models to predict the *EA* and *PCF* is verified again to guarantee the effectiveness of the optimization method. It is found that the mass of the optimized structure increases from 0.3237 to 0.4916 kg by 50%. Even though there is a small increment on the mass, the optimized C-NPR-IT improves *EA* from 1.28 to 4.95 kJ by almost 2.5 times indicating the optimized structure is a better energy absorber. As given in Table 4, it is noticeable that the errors between FEM and RBF modeling optimization results are all less than 5%, indicating that the RBF models achieve good accuracy.

6 Conclusion

The proposed C-NPR-IT structure can take the advantage of both NPR structures and thin-walled tubes on the energy absorption performance. Compared to the interaction between NPR structure and thin-walled tubes in C-NPR-OT structure, it has been enhanced by efficiently utilizing the negative Poisson's ratio property. The geometric parameters nl , nc , t_s , t_l , r_i have great effects on the crashworthiness performance. It is found that the effects are strongly nonlinear to design the suitable structure. RBF surrogate model and multi-objective optimization algorithm (MOPSO) are utilized to achieve the optimal C-NPR-IT structure, which has the higher *EA* and lower *PCF*. The optimized structure prefers to have larger *SEA* and smaller *PCF*. *EA* increases from 1.28 to 4.95 kJ by almost 2.5 times. The study indicates the C-NPR-IT has tremendous application potential in the energy absorber field. However, this paper only focuses on the numerical simulations of the hybrid structures under axial impact loading. In the future work, more experiments will be conducted, and an analytical formula will be developed to predict the energy absorption. Also, the crashworthiness performance of the structure proposed under oblique impact loading will be investigated.

Supplementary Information The online version contains supplementary material available at <https://doi.org/10.1007/s00158-021-03071-2>.

Acknowledgements This work was supported by the National Science and Technology Major Special Project, Demonstration Project of Precision Forming and Processing Equipment for Axle Parts of Transmission (2018ZX04024001), National Science Foundation for Young Scientist of China (51605195) and Fundamental Research Funds for the Central Universities (30919011203, 30919011203B8809), as well as the Research Grants Council of the Hong Kong Special Administrative Region, China (Project No. CUHK14202219) and the Chinese University of Hong Kong (Project ID: 4055117).

Declarations

Conflict of interest The authors declared that they have no conflicts of interest to this work.

Replication of results The raw data for Figs. 5, 8, 9, 10, 11, 12 and 14 are given in Figs. 5.xlsx, 8.xlsx, 9.xlsx, 10.xlsx, 11.xlsx, 12.xlsx and 14.xlsx. The other data are detailed in the paper.

References

- Abdullahi HS, Gao S (2020) A two-stage approach to the optimization design of multi-cell square tubal structures. *Struct Multidisc Optim*. <https://doi.org/10.1007/s00158-020-02735-9>
- Abramowicz W, Jones N (1986) Dynamic progressive buckling of circular and square tubes. *Int J Impact Eng* 4:243–270. [https://doi.org/10.1016/0734-743X\(86\)90017-5](https://doi.org/10.1016/0734-743X(86)90017-5)
- Acar E, Altin M, Güler MA (2019) Evaluation of various multi-cell design concepts for crashworthiness design of thin-walled aluminum tubes. *Thin-Walled Struct* 142:227–235. <https://doi.org/10.1016/j.tws.2019.05.012>
- Alderson A, Alderson KL, Attard D, Evans KE, Gatt R, Grima JN, Müller W, Ravirala N, Smith W, Zied K (2010) Elastic constants of 3-, 4- and 6-connected chiral and anti-chiral honeycombs subject to uniaxial in-plane loading. *Compos Sci Technol* 70:1042–1048. <https://doi.org/10.1016/j.compscitech.2009.07.009>
- Altin M, Kılınçkaya Ü, Acar E, Güler MA (2019) Investigation of combined effects of cross section, taper angle and cell structure on crashworthiness of multi-cell thin-walled tubes. *Int J Crashworthiness* 24:121–136. <https://doi.org/10.1080/13588265.2017.1410338>
- Altinay M (2019) Investigation of performances of energy absorbing profiles having different geometries under oblique loads. *J Fac Eng Archit Gazi Univ* 34:1517–1526
- An X, Gao Y, Fang J, Sun G, Li Q (2015) Crashworthiness design for foam-filled thin-walled structures with functionally lateral graded thickness sheets. *Thin-Walled Struct* 91:63–71. <https://doi.org/10.1016/j.tws.2015.01.011>
- Baykasoğlu A, Baykasoğlu C, Cetin E (2020) Multi-objective crashworthiness optimization of lattice structure filled thin-walled tubes. *Thin-Walled Struct* 149:106630. <https://doi.org/10.1016/j.tws.2020.106630>
- Cetin E, Baykasoğlu C (2019) Energy absorption of thin-walled tubes enhanced by lattice structures. *Int J Mech Sci* 157–158:471–484. <https://doi.org/10.1016/j.ijmecsci.2019.04.049>
- Duan L, Jiang H, Geng G, Zhang X, Li Z (2019) Parametric modeling and multiobjective crashworthiness design optimization of a new front longitudinal beam. *Struct Multidisc Optim* 59:1789–1812. <https://doi.org/10.1007/s00158-018-2134-9>
- Duc ND, Seung-Eock K, Tuan ND, Tran P, Khoa ND (2017) New approach to study nonlinear dynamic response and vibration of sandwich composite cylindrical panels with auxetic honeycomb core layer. *Aerosp Sci Technol* 70:396–404. <https://doi.org/10.1016/j.ast.2017.08.023>
- Elipe JCA, Lantada AD (2012) Comparative study of auxetic geometries by means of computer-aided design and engineering. *Smart Mater Struct* 21:105004. <https://doi.org/10.1088/0964-1726/21/10/105004>
- Evans KE (1991) Auxetic polymers: a new range of materials. *Endeavour* 15:170–174. [https://doi.org/10.1016/0160-9327\(91\)90123-S](https://doi.org/10.1016/0160-9327(91)90123-S)
- Ferguson, W. J., Kuang, Y., Evans, K. E., Smith, C. W., & Zhu, M (2018) Auxetic structure for increased power output of strain

- vibration energy harvester. *Sens Actuators Phys* 282:90–96. <https://doi.org/10.1016/j.sna.2018.09.019>
- Fu M, Liu F, Hu L (2018) A novel category of 3D chiral material with negative Poisson's ratio. *Compos Sci Technol* 160:111–118. <https://doi.org/10.1016/j.compscitech.2018.03.017>
- Gao Q, Wang L, Wang Y, Guo F, Zhang Z (2016) Optimization of foam-filled double ellipse tubes under multiple loading cases. *Adv Eng Softw* 99:27–35. <https://doi.org/10.1016/j.advengsoft.2016.05.001>
- Gao Q, Wang L, Wang Y, Guo F, Zhang Z (2018a) Theoretical, numerical and experimental analysis of three-dimensional double-V honeycomb. *Mater Des* 139:380–391. <https://doi.org/10.1016/j.matdes.2017.11.024>
- Gao Q, Zhao X, Wang C, Wang L, Ma Z (2018b) Multi-objective crashworthiness optimization for an auxetic cylindrical structure under axial impact loading. *Mater Des* 143:120–130. <https://doi.org/10.1016/j.matdes.2018.01.063>
- Gao Q, Ge C, Zhuang W, Wang L, Ma Z (2019) Crashworthiness analysis of double-arrowed auxetic structure under axial impact loading. *Mater Des* 161:22–34. <https://doi.org/10.1016/j.matdes.2018.11.013>
- Gibson LJ, Ashby MF (1999) *Cellular Solids: Structure and Properties*. Cambridge University Press, Cambridge
- Hu LL, Yu TX (2013) Mechanical behavior of hexagonal honeycombs under low-velocity impact—theory and simulations. *Int J Solids Struct* 50:3152–3165. <https://doi.org/10.1016/j.ijsolstr.2013.05.017>
- Huang H, Xu S (2019) Crashworthiness analysis and bionic design of multi-cell tubes under axial and oblique impact loads. *Thin-Walled Struct* 144:106333. <https://doi.org/10.1016/j.tws.2019.106333>
- Imbalzano G, Tran P, Ngo TD, Lee PV (2017) Three-dimensional modelling of auxetic sandwich panels for localised impact resistance. *J Sandw Struct Mater* 19:291–316
- Jiang L, Hu H (2017) Low-velocity impact response of multilayer orthogonal structural composite with auxetic effect. *Compos Struct* 169:62–68. <https://doi.org/10.1016/j.compstruct.2016.10.018>
- Jin R, Chen W, Sudjianto A (2005) An efficient algorithm for constructing optimal design of computer experiments. *J Stat Plan Inference* 134:268–287. <https://doi.org/10.1016/j.jspi.2004.02.014>
- Kitayama S, Arakawa M, Yamazaki K (2006) Penalty function approach for the mixed discrete nonlinear problems by particle swarm optimization. *Struct Multidisc Optim* 32:191–202. <https://doi.org/10.1007/s00158-006-0021-2>
- Lakes R (1987) Foam structures with a negative Poisson's ratio. *Science* 235:1038–1041
- Lan X, Feng S, Huang Q, Zhou T (2019) A comparative study of blast resistance of cylindrical sandwich panels with aluminum foam and auxetic honeycomb cores. *Aerosp Sci Technol* 87:37–47. <https://doi.org/10.1016/j.ast.2019.01.031>
- Li G, Zhang Z, Sun G, Xu F, Huang X (2014) Crushing analysis and multiobjective optimization for functionally graded foam-filled tubes under multiple load cases. *Int J Mech Sci* 89:439–452. <https://doi.org/10.1016/j.ijmecsci.2014.10.001>
- Li X, Wang Q, Yang Z, Lu Z (2019) Novel auxetic structures with enhanced mechanical properties. *Extreme Mech Lett* 27:59–65. <https://doi.org/10.1016/j.eml.2019.01.002>
- Lu Z, Wang Q, Li X, Yang Z (2017) Elastic properties of two novel auxetic 3D cellular structures. *Int J Solids Struct* 124:46–56. <https://doi.org/10.1016/j.ijsolstr.2017.05.031>
- Mohammadiha O, Ghariblu H (2017) Optimal shape design of functionally graded thickness inversion tubes subjected to oblique loading. *Struct Multidisc Optim* 56:587–601. <https://doi.org/10.1007/s00158-017-1676-6>
- Nikkhah H, Baroutaji A, Olabi AG (2019) Crashworthiness design and optimisation of windowed tubes under axial impact loading. *Thin-Walled Struct* 142:132–148. <https://doi.org/10.1016/j.tws.2019.04.052>
- Novak N, Starčević L, Vesenjanić M, Ren Z (2019) Blast response study of the sandwich composite panels with 3D chiral auxetic core. *Compos Struct* 210:167–178. <https://doi.org/10.1016/j.compstruct.2018.11.050>
- Pirmohammad S, Esmaeili-Marzdashti S (2019) Multi-objective crashworthiness optimization of square and octagonal bitubal structures including different hole shapes. *Thin-Walled Struct* 139:126–138. <https://doi.org/10.1016/j.tws.2019.03.004>
- Qi C, Yang S, Dong F (2012) Crushing analysis and multiobjective crashworthiness optimization of tapered square tubes under oblique impact loading. *Thin-Walled Struct* 59:103–119. <https://doi.org/10.1016/j.tws.2012.05.008>
- Qiu N, Gao Y, Fang J, Feng Z, Sun G, Li Q (2016) Theoretical prediction and optimization of multi-cell hexagonal tubes under axial crushing. *Thin-Walled Struct* 102:111–121. <https://doi.org/10.1016/j.tws.2016.01.023>
- Qiu N, Gao Y, Fang J, Sun G, Kim NH (2018) Topological design of multi-cell hexagonal tubes under axial and lateral loading cases using a modified particle swarm algorithm. *Appl Math Model* 53:567–583. <https://doi.org/10.1016/j.apm.2017.08.017>
- Ren X, Das R, Tran P, Ngo TD, Xie YM (2018) Auxetic metamaterials and structures: a review. *Smart Mater Struct* 27:023001. <https://doi.org/10.1088/1361-665X/aaa61c>
- Shang X, Chao T, Ma P, Yang M (2020) An efficient local search-based genetic algorithm for constructing optimal Latin hypercube design. *Eng Optim* 52:271–287. <https://doi.org/10.1080/0305215X.2019.1584618>
- Simpson J, Kazancı Z (2020) Crushing investigation of crash boxes filled with honeycomb and re-entrant (auxetic) lattices. *Thin-Walled Struct* 150:106676. <https://doi.org/10.1016/j.tws.2020.106676>
- Sun G, Li G, Zhou S, Li H, Hou S, Li Q (2011) Crashworthiness design of vehicle by using multiobjective robust optimization. *Struct Multidisc Optim* 44:99–110. <https://doi.org/10.1007/s00158-010-0601-z>
- Usta F, Ertaş OF, Ataalp A, Türkmen HS, Kazancı Z, Scarpa F (2018) Impact behavior of triggered and non-triggered crash tubes with auxetic lattices. *Multiscale Multidiscip Model Exp Des*. <https://doi.org/10.1007/s41939-018-00040-z>
- Wang Y, Wang L, Ma Z, Wang T (2016) A negative Poisson's ratio suspension jounce bumper. *Mater Des* 103:90–99. <https://doi.org/10.1016/j.matdes.2016.04.041>
- Wang C, Wang W, Zhao W, Wang Y, Zhou G (2018a) Structure design and multi-objective optimization of a novel NPR bumper system. *Compos Part B Eng* 153:78–96. <https://doi.org/10.1016/j.compositesb.2018.07.024>
- Wang Y, Zhao W, Zhou G, Gao Q, Wang C (2018b) Optimization of an auxetic jounce bumper based on Gaussian process metamodel and series hybrid GA-SQP algorithm. *Struct Multidisc Optim* 57:2515–2525. <https://doi.org/10.1007/s00158-017-1869-z>
- Wang Y, Zhao W, Zhou G, Gao Q, Wang C (2018c) Suspension mechanical performance and vehicle ride comfort applying a novel jounce bumper based on negative Poisson's ratio structure. *Adv Eng Softw* 122:1–12. <https://doi.org/10.1016/j.advengsoft.2018.04.001>
- Wu S, Zheng G, Sun G, Liu Q, Li G, Li Q (2016) On design of multi-cell thin-wall structures for crashworthiness. *Int J Impact Eng* 88:102–117. <https://doi.org/10.1016/j.ijimpeng.2015.09.003>
- Xie S, Li H, Yang W, Wang N (2018) Crashworthiness optimisation of a composite energy-absorbing structure for railway vehicles. *Struct Multidisc Optim* 57:1793–1807. <https://doi.org/10.1007/s00158-017-1829-7>

- Xiong F, Wang D, Chen S, Gao Q, Tian S (2018) Multi-objective lightweight and crashworthiness optimization for the side structure of an automobile body. *Struct Multidisc Optim* 58:1823–1843. <https://doi.org/10.1007/s00158-018-1986-3>
- Yang H, Wang B, Ma L (2019) Mechanical properties of 3D double-U auxetic structures. *Int J Solids Struct* 180–181:13–29. <https://doi.org/10.1016/j.ijsolstr.2019.07.007>
- Yin H, Wen G, Liu Z, Qing Q (2014) Crashworthiness optimization design for foam-filled multi-cell thin-walled structures. *Thin-Walled Struct* 75:8–17. <https://doi.org/10.1016/j.tws.2013.10.022>
- Zhang J, Lu G, Ruan D, Wang Z (2018) Tensile behavior of an auxetic structure: analytical modeling and finite element analysis. *Int J Mech Sci* 136:143–154. <https://doi.org/10.1016/j.ijmecsci.2017.12.029>
- Zhang Y, Sun G, Li G, Luo Z, Li Q (2012) Optimization of foam-filled bitubal structures for crashworthiness criteria. *Mater Des* 38:99–109. <https://doi.org/10.1016/j.matdes.2012.01.028>
- Zhao X, Gao Q, Wang L, Yu Q, Ma ZD (2018) Dynamic crushing of double-arrowed auxetic structure under impact loading. *Mater Des* 160:527–537. <https://doi.org/10.1016/j.matdes.2018.09.041>
- Zhou G, Ma ZD, Li G, Cheng A, Duan L, Zhao W (2016) Design optimization of a novel NPR crash box based on multi-objective genetic algorithm. *Struct Multidisc Optim* 54:673–684. <https://doi.org/10.1007/s00158-016-1452-z>
- Zhu G, Sun G, Li G, Cheng A, Li Q (2018a) Modeling for CFRP structures subjected to quasi-static crushing. *Compos Struct* 184:41–55. <https://doi.org/10.1016/j.compstruct.2017.09.001>
- Zhu G, Sun G, Yu H, Li S, Li Q (2018b) Energy absorption of metal, composite and metal/composite hybrid structures under oblique crushing loading. *Int J Mech Sci* 135:458–483. <https://doi.org/10.1016/j.ijmecsci.2017.11.017>

Publisher's Note Springer Nature remains neutral with regard to jurisdictional claims in published maps and institutional affiliations.